APPENDIX

In this Appendix, we compute the eigenvectors and the eigenvalues of matrix **L** as defined by Eq. (8). Let the column vector **v** with column element v_n be an eigenvector of the matrix **L**, with eigenvalue λ. It follows that

$$v_{n-1} - \beta v_n + v_{n+1} = -\delta^2 \lambda v_n, \qquad \text{for } n = 1, 2, 3, \ldots, N \tag{31}$$

with $v_0 = v_N$ and $v_1 = v_{N+1}$. In order to solve above difference equation, one assumes that the components of the eigenvectors take the form

$$v_n = a\alpha^{-n} + b\alpha^n \tag{32}$$

where the constants a and b are to be chosen in such a way that the periodicity condition $v_j = v_{N+j}$, for $j = 0, 1, 2, \ldots,$ is satisfied. Substitution of Eq. (32) into Eq. (31) leads to

$$-\delta^2 \lambda = \alpha^{-1} - \beta + \alpha. \tag{33}$$

Making use of the periodicity condition, we find the eigenvalues and eigenvectors of **L**:

$$\alpha_m = e^{i(2m\pi/N)}, \qquad \lambda_m = \frac{4}{\delta^2} \sin^2 \frac{m\pi}{N} - \frac{1}{4}, \quad \text{and}$$
$$v_{n,m} = a_m e^{-i(2mn\pi/N)} + b_m e^{i(2mn\pi/N)}, \qquad m, n = 1, 2, \ldots, N \tag{34}$$

where a_m and b_m are constants. The desire to work with real matrices dictates that we choose

$$b_m = \begin{cases} a_m = \dfrac{1}{\sqrt{2N}}, & \text{if } m = 1, 2, \ldots, (N-1)/2 \\ -a_m = \dfrac{1}{\sqrt{2N}}, & \text{if } m = (N+1)/2, \ldots, (N-1) \\ -a_m + \dfrac{1}{\sqrt{N}}, & \text{if } m = N. \end{cases} \tag{35}$$

With the above chosen constants, we can show that $P^{-1} = P^T$. To prove this statement, it is sufficient to note that

$$\begin{aligned} (PP^T)_{nm} &= \sum_{k=1}^{N} v_{nk} v_{mk} \\ &= v_{nN} v_{mN} + \sum_{k=1}^{(N-1)/2} v_{nk} v_{mk} + \sum_{k=(N+1)/2}^{N-1} v_{nk} v_{mk} \\ &= \frac{1}{N} \sum_{k=0}^{N} \cos \frac{2k(n-m)\pi}{N} \\ &\quad + \frac{1}{N} \sum_{k=1}^{(N-1)/2} \cos \frac{2k(n+m)\pi}{N} \\ &\quad - \frac{1}{N} \sum_{k=(N+1)/2}^{N-1} \cos \frac{2k(n+m)\pi}{N} \\ &= \frac{1}{N} \sum_{k=0}^{N} \cos \frac{2k(n-m)\pi}{N} \\ &\quad + \frac{1}{N} \sum_{k=1}^{(N-1)/2} \left[\cos \frac{2k(n+m)\pi}{N} \right. \\ &\quad \left. - \cos \frac{2(N-k)(n+m)\pi}{N} \right] \\ &= \frac{1}{N} \text{Real} \left[\sum_{k=0}^{N-1} e^{i(2(n-m)k\pi/N)} \right] = \delta_{nm}. \end{aligned} \tag{36}$$

REFERENCES

1. K. Chadan and P.C. Sabatier, Inverse problems in quantum scattering theory, Springer-Verlag, New York, 1989, 2nd ed.
2. B.N. Zakhariev and A.A. Suzko, Direct and inverse problems, Springer-Verlag, New York, 1990.
3. D. Colton and R. Kress, Inverse acoustic and electromagnetic scattering theory, Springer-Verlag, New York, 1992.
4. G. Meyer, The method of lines for Poisson's equation with nonlinear or free boundary conditions, Numer Math 29 (1978), 329–344.
5. J.G. Ma, T.K. Chia, T.W. Tan, and K.Y. See, Electromagnetic wave scattering from 2-D cylinder by using the method of lines, Microwave Opt Technol Lett 24 (2000), 275–277.
6. J.A. Kong, Electromagnetic Wave Theory, Wiley, New York, 1990, 2nd ed.
7. D. Zwillinger, Handbook of differential equations, Academic, New York, 1989.
8. E. Isaacson and H.B. Keller, Analysis of numerical methods, Wiley, New York, 1966.
9. N. Bleistein, Mathematical methods for wave phenomena, Academic, New York, 1984.
10. G.F. Forsythe, M.A. Malcolm, and C.B. Moler, Computer methods for mathematical computations, Prentice-Hall, New York, 1976.

WIND DIRECTION AZIMUTHAL SIGNATURE IN THE STOKES EMISSION VECTOR FROM THE OCEAN SURFACE AT MICROWAVE FREQUENCIES

A. J. Camps[1] and S. C. Reising[2]
[1] Department of Signal Theory and Communications
Universitat Politècnica de Catalunya
08034 Barcelona, Spain
[2] Microwave Remote Sensing Laboratory
Department of Electrical and Computer Engineering
University of Massachusetts
Amherst, Massachusetts 01003

Received 10 January 2001

ABSTRACT: *An ocean polarimetric emission model is presented. It is found that skewness and upwind/cross-wind rms slopes are responsible for the first and second azimuthal harmonic, respectively. Atmospheric effects contribute significantly at low wind speeds, and at horizontal polarization at certain observation angles. Simulation results compare favorably with reported JPL–WINDRAD measurements.* © 2001 John Wiley & Sons, Inc. Microwave Opt Technol Lett 29: 426–432, 2001.

Key words: *microwave; radiometry; polarimetry; wind; ocean*

1. INTRODUCTION

Ocean wind speed and direction maps are routinely computed from wind scatterometer data. Wind-speed maps are

Contract grant sponsor: Spanish Ministry of Education and Culture
Contract grant number: Fellowship PR98 0046131105

also routinely derived from vertical and horizontal microwave brightness temperatures. In 1992, Wentz [1] found small wind-direction signatures in SSM/I vertical and horizontal brightness temperatures, and during the 1990s, airborne measurements showed wind-direction signatures in the four Stokes elements [2–5]. In the near future, spaceborne polarimetric radiometers will be launched [6].

Several approaches are found in the literature to compute the azimuthal emission signature of a rough surface: the two-scale/small-perturbation model (SPM) [7], the small-slope expansion [8, 9], Monte Carlo simulations using geometric optics (GO) [10], and the method of moments [11]. Irisov [8] showed that the SPM and the small-slope expansion method are identical. Strictly speaking, the SPM is accurate at low frequencies, when $k\sigma \leq 0.3$ (k: wavenumber, σ: rms height), while GO is accurate at high frequencies [10]. Two-scale models are probably the most frequently used, and they rely on the choice of a proper cutoff wavenumber k_d [12]. This paper improves the analytical model by Stogryn [13] based on the Kirchhoff method under the stationary phase approximation to include skewness and peakedness effects, in addition to the asymmetry between upwind and cross-wind rms slopes.

This paper is divided into five sections. Section 2 reviews basic polarimetric radiometry concepts, and introduces the Stokes vector. Section 3 describes the model, discusses the effects of different upwind and cross-wind rms slopes, skewness, and peakedness terms, two foam models, and atmospheric effects. Section 4 presents model predictions at 37 GHz for different wind speeds and incidence angles. Finally, Section 5 presents the comparisons between model results and JPL–WINDRAD measurements.

2. REVIEW OF BASIC POLARIMETRIC RADIOMETRY CONCEPTS

The thermal emission from a surface bounding a semi-infinite volume at a constant temperature T_s, in the direction (θ, ϕ), is described by the Stokes vector [3]

$$\begin{bmatrix} T_h(\theta,\phi) \\ T_v(\theta,\phi) \\ U(\theta,\phi) \\ V(\theta,\phi) \end{bmatrix} = T_s \begin{bmatrix} e_h(\theta,\phi) \\ e_v(\theta,\phi) \\ e_U(\theta,\phi) \\ e_V(\theta,\phi) \end{bmatrix} = C \begin{bmatrix} \langle E_h E_h^* \rangle \\ \langle E_v E_v^* \rangle \\ 2\,\mathrm{Re}\langle E_v E_h^* \rangle \\ 2\,\mathrm{Im}\langle E_v E_h^* \rangle \end{bmatrix} \quad (1)$$

where T_h and T_v are the horizontal (h) and vertical (v) brightness temperatures, U and V are the third and fourth Stokes parameters formed from the real (Re) and imaginary (Im) parts of the complex cross correlation of the electric fields emitted by the surface at horizontal (E_h) and vertical (E_v) polarizations, $\langle\ \rangle$ is the expectation operator, C is an instrument-dependent constant, and e_h, e_v, e_U, e_V are their emissivities.

The emissivities of an irregular surface in the XY-plane at h and v polarizations, observed from an observation angle θ (relative to 0° at nadir) and an azimuth angle ϕ (relative to 0° in the direction of the wind), are related to its scattering properties by [3, 14]

$$\begin{bmatrix} e_h(\theta,\phi) \\ e_v(\theta,\phi) \\ e_U(\theta,\phi) \\ e_V(\theta,\phi) \end{bmatrix} = \begin{bmatrix} 1 \\ 1 \\ 0 \\ 0 \end{bmatrix} - \frac{1}{4\pi\cos\theta} \iint_{2\pi} \cos\theta_i \begin{bmatrix} \gamma_{hhhh}(\theta,\phi,\theta_i\phi_i) + \gamma_{hvhv}(\theta,\phi,\theta_i,\phi_i) \\ \gamma_{vvvv}(\theta,\phi,\theta_i,\phi_i) + \gamma_{vhvh}(\theta,\phi,\theta_i,\phi_i) \\ 2\,\mathrm{Re}(\gamma_{vhhh}(\theta,\phi,\theta_i,\phi_i) + \gamma_{vvhv}(\theta,\phi,\theta_i,\phi_i)) \\ 2\,\mathrm{Im}(\gamma_{vhhh}(\theta,\phi,\theta_i,\phi_i) + \gamma_{vvhv}(\theta,\phi,\theta_i,\phi_i)) \end{bmatrix} d\Omega_i \quad (2)$$

where the polarimetric bistatic scattering coefficients $\gamma_{mnpq}(\theta, \phi, \theta_i, \phi_i)$ describe the scattering in the direction (θ, ϕ) of a wave incident from the direction (θ_i, ϕ_i). The coefficient γ_{mnpq} describes the resulting cross correlation of the scattered waves at m and p polarizations due to incident waves at n and q polarizations, respectively.

3. DESCRIPTION OF THE MODEL

The polarimetric bistatic scattering coefficients in Eq. (2) are derived following a procedure similar to Stogryn [13, 15]:

$$\begin{aligned} \gamma_{mnpq}(\theta,\phi,\theta_i,\phi_i) &= \frac{1}{\cos\theta_i} \frac{k^2 q^2 U_{mn} U_{pq}^*}{2 q_z^4 \sigma_u \sigma_c} \exp\left[-\frac{1}{2 q_z^2} \left(\frac{q_x^2}{\sigma_u^2} + \frac{q_y^2}{\sigma_c^2} \right) \right] \\ &\times \left\{ 1 - \frac{1}{2} c_{21} \left(\left(\frac{q_y}{\sigma_c} \right)^2 - 1 \right) \frac{q_x}{\sigma_u} \right. \\ &- \frac{1}{6} c_{03} \left(\left(\frac{q_x}{\sigma_u} \right)^3 - 3 \frac{q_x}{\sigma_u} \right) \\ &+ \frac{1}{24} c_{40} \left(\left(\frac{q_y}{\sigma_c} \right)^4 - 6 \left(\frac{q_y}{\sigma_c} \right)^2 + 3 \right) \\ &+ \frac{1}{4} c_{22} \left(\left(\frac{q_y}{\sigma_c} \right)^2 - 1 \right) \left(\left(\frac{q_x}{\sigma_u} \right)^2 - 1 \right) \\ &\left. + \frac{1}{24} c_{04} \left(\left(\frac{q_x}{\sigma_u} \right)^4 - 6 \left(\frac{q_x}{\sigma_u} \right)^2 + 3 \right) \right\}. \end{aligned} \quad (3)$$

The ocean surface slopes are described by a Gram–Charlier pdf [16], including different upwind ($+x$, $\phi = 0°$) and cross-wind (y) rms slopes ($\sigma_u^2 = 0.00316w$ and $\sigma_c^2 = 0.003 + 0.00192w$, w: wind speed measured at 12.5 m height), skewness ($c_{21} = 0.01 - 0.0086w$, $c_{03} = 0.04 - 0.033w$), and peakedness ($c_{40} = 0.40$, $c_{22} = 0.12$, and $c_{04} = 0.23$) terms. Wilheit's [16] frequency corrections for the rms slopes have been included ($0.3 + 0.02 f_{[\mathrm{GHz}]}$, $f < 35$ GHz). Multiple scattering and surface shadowing effects are not included. The validity of GO methods applied to the ocean surface depends on wind speed, observation angle, and frequency. For example, at 37 GHz, it can be applied for all wind speeds up to 24 m/s at $\theta = 30°$, and up to about 9 m/s at $\theta = 60°$ [10].

3.1. Skewness and Peakedness Effects. Figure 1(a)–(c) shows the azimuthal dependence of $\Delta T_v(\theta, \phi)$, $\Delta T_h(\theta, \phi)$, and $U(\theta, \phi)$ at $\theta = 53.1°$ and $w = 7.9$ m/s on the upwind/cross-wind asymmetry $\sigma_u^2 \neq \sigma_c^2$ (dotted line), also when skewness

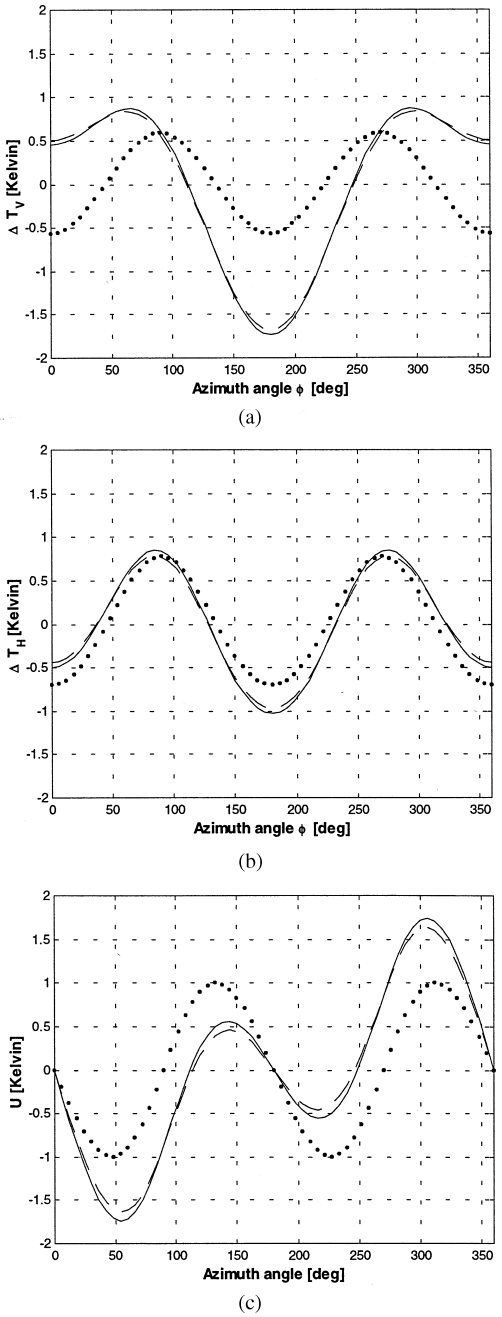

Figure 1 Azimuthal signatures in (a) T_v, (b) T_h, and (c) U induced by the upwind/cross-wind asymmetry (dotted line), also including skewness effects (dashed line) and peakedness effects (solid line) at $\theta = 53.1°$ and $w = 7.9$ m/s, with SST = 12°C and SSS = 33 psu

coefficients c_{21} and c_{03} are included (dashed line), and finally when all of the previous effects and the peakedness coefficients c_{40}, c_{22}, and c_{04} are included (solid line). To show more clearly the impact of these parameters, foam and atmospheric effects have not been included. As shown in Figure 1, when only σ_u^2, σ_c^2 are considered (dotted line), $\Delta T_v(\theta, \phi)$ and $\Delta T_h(\theta, \phi)$ have an azimuthal dependence as $\cos(2\phi)$, while $U(\theta, \phi)$ is proportional to $\sin(2\phi)$. When the skewness terms are taken into account (dashed line), a first-harmonic dependence as $\cos(\phi)$ is observed for $\Delta T_v(\theta, \phi)$ and $\Delta T_h(\theta, \phi)$, and as $\sin(\phi)$ for $U(\theta, \phi)$. Taking into account the peakedness coefficients (solid line) introduces a minor change in the shape of the azimuthal dependence, and can be neglected in Eq. (3).

3.2. Foam Coverage Effects. Two foam coverage models have been analyzed in this study: a uniform-cover, polarization-insensitive model [16], and a dynamic-foam model [10] with different vertical and horizontal foam emissivities [18]. No significant differences have been found [19], and therefore the uniform model has been implemented for simplicity. Other sources of uncertainty in the modeling of sea foam have been reported. Monahan and Lu [20] have indicated that foam may appear at lower wind speeds, about 3–4 m/s, and Monahan and O'Muircheartaigh [21] have evidence that the whitecap coverage depends not only on wind speed, but also on atmospheric stability $\Delta T = T_{\text{water}} - T_{\text{atm}}$ (by $\pm 9\%$ for $\Delta T = \pm 1°\text{C}$), water temperature T_{water} (water viscosity changes with T_{water}), wind duration, fetch, and water salinity (51% larger whitecap coverage on the sea than on fresh water).

3.3. Atmospheric Effects. Two main effects produced by the atmosphere have been reported in the literature: atmospheric stability (ΔT) and attenuation. In addition to its impact on whitecap coverage, atmospheric stability affects the wind-speed height profile, the mean wind speed at the surface, and the sea-scattering coefficients. Atmospheric attenuation produces a depolarization of the radiation reaching the radiometer, and a decrease of the amplitude of the harmonics of T_h, T_v, and U [22].

A third effect is the induced polarization and azimuthal dependence of the downwelling temperature $T_{DNh,v}$ (atmospheric + galactic + cosmic noise) scattered from the ocean surface that is then measured by the radiometer. Assuming an azimuthally symmetric scatter-free atmosphere $T_{UPh}(\theta) = T_{UPv}(\theta)$, $T_{DNh}(\theta) = T_{DNv}(\theta) \triangleq T_{DN}(\theta)$, and $U_{UP} = V_{UP} = U_{DN} = V_{DN} = 0$,

$$T_{AP_v^h}(\theta, \phi) = \left[e_{\substack{h \\ v}}(\theta, \phi) T_s + T_{sc_v^h}(\theta, \phi) \right] e^{-\tau(\theta)} + T_{UP}(\theta)$$

$$\begin{matrix} U_{AP} \\ V_{AP} \end{matrix}(\theta, \phi) = \left[e_{\substack{U \\ V}}(\theta, \phi) T_s + \begin{matrix} U_{sc} \\ V_{sc} \end{matrix}(\theta, \phi) \right] e^{-\tau(\theta)} \tag{4}$$

$$\begin{bmatrix} T_{sch} \\ T_{scv} \\ U_{sc} \\ V_{sc} \end{bmatrix} = \frac{1}{4\pi \cos\theta} \iint_{2\pi} \cos\theta_i \begin{bmatrix} \gamma_{hhhh} + \gamma_{hvhv} \\ \gamma_{vvvv} + \gamma_{vhvh} \\ 2\,\text{Re}(\gamma_{vhhh} + \gamma_{vvhv}) \\ 2\,\text{Im}(\gamma_{vhhh} + \gamma_{vvhv}) \end{bmatrix} \times T_{DN}(\theta)\, d\Omega_i \tag{5}$$

where the subscripts *AP*, *UP*, *DN*, and *sc* indicate apparent, upwelling, downwelling, and scattered temperatures, respectively, and $\tau(\theta)$ is the opacity of the atmosphere. The angular and frequency dependences in Eqs. (4) and (5) have been omitted for simplicity. In the presence of hydrometeors (rain, ice, etc.), the atmospheric upwelling and downwelling emission may already be polarized ($T_{UPh} \neq T_{UPv}$; $T_{DNh} \neq T_{DNv}$; $U_{UP}, U_{DN}, V_{UP}, V_{DN} \neq 0$) [23], and scattering from the ocean surface changes its polarization state, and (5) becomes

$$\begin{bmatrix} T_{sch} \\ T_{scv} \\ U_{sc} \\ V_{sc} \end{bmatrix} = \frac{1}{4\pi \cos\theta} \iint_{2\pi} \cos\theta_i \begin{bmatrix} \gamma_{hhhh} & \gamma_{hvhv} & \mathrm{Re}(\gamma_{hvhh}) & -\mathrm{Im}(\gamma_{hvhh}) \\ \gamma_{vhvh} & \gamma_{vvvv} & \mathrm{Re}(\gamma_{vvvh}) & -\mathrm{Im}(\gamma_{vvvh}) \\ 2\,\mathrm{Re}(\gamma_{vhhh}) & 2\,\mathrm{Re}(\gamma_{vvhv}) & \mathrm{Re}(\gamma_{vvhh} + \gamma_{vhhv}) & -\mathrm{Im}(\gamma_{vvhh} - \gamma_{vhhv}) \\ 2\,\mathrm{Im}(\gamma_{vhhh}) & 2\,\mathrm{Im}(\gamma_{vvhv}) & \mathrm{Im}(\gamma_{vvhh} + \gamma_{vhhv}) & \mathrm{Re}(\gamma_{vvhh} - \gamma_{vhhv}) \end{bmatrix} \begin{bmatrix} T_{DNh}(\theta) \\ T_{DNv}(\theta) \\ U_{DN}(\theta) \\ V_{DN}(\theta) \end{bmatrix} d\Omega_i \quad (6)$$

which reduces to Eq. (5) when $T_{DNh} = T_{DNv} = T_{DN}$ and $U_{UP} = V_{DN} = 0$. The azimuthal dependence of T_{sch}, T_{scv}, U_{sc}, and V_{sc} in Eq. (6) is out of phase with that of the surface's emission in Eq. (2) (Fig. 2). These effects will normally tend to compensate each other, reducing the magnitude of this azimuthal signature, except when it is very small (horizontal polarization at $\theta \sim 45°$ or low wind speeds)

4. MODEL PREDICTIONS

The angular dependence of the Stokes elements can be expressed by

$$\begin{aligned} T_h(\theta, \phi) &= T_{h0}(\theta) + T_{h1}(\theta)\cos\phi + T_{h2}(\theta)\cos(2\phi) \\ T_v(\theta, \phi) &= T_{v0}(\theta) + T_{v1}(\theta)\cos\phi + T_{v2}(\theta)\cos(2\phi) \\ U(\theta, \phi) &= U_1(\theta)\sin\phi + U_2(\theta)\sin(2\phi). \end{aligned} \quad (7)$$

Figure 2(a) and (b) shows the dependence of $T_{h0}(\theta)$ and $T_{v0}(\theta)$ on the observation angle at 37 GHz for wind speeds of 5, 10, and 15 m/s. At nadir, the sensitivity to wind speed is approximately 0.6–1 K/(m/s), depending on the wind speed, and is null around 53° at vertical polarization. Results from Wentz's SSM/I geophysical model function at 53.1° are shown with crosses for comparison [1]. Figure 2(c)–(n) shows that the amplitudes of the azimuthal harmonics T_{h1}, T_{v1}, U_1, T_{h2}, T_{v2}, and U_2 of the ocean emission have been numerically computed at 37 GHz and $w = 5$, 10, and 15 m/s. Other parameters are 12°C sea-surface temperature and 36 psu sea-surface salinity. The amplitudes of the scattered downwelling atmospheric temperature have also been computed, and are plotted in Figure 2 for comparison. As commented on in Section 3, they are out of phase with their corresponding emission harmonics, thus reducing the total azimuthal signature. As can be appreciated, the first harmonic is zero at nadir ($\theta = 0°$), and its amplitude increases with the incidence angle, for which skewness effects are more noticeable. On the other hand, the second harmonic vanished around 40–50° incidence angle, depending on the wind speed. At these angles, and at low wind speeds, the first harmonic is also very small, and the azimuthal signature is dominated by the scattered downwelling atmospheric temperature.

5. COMPARISON WITH REPORTED EXPERIMENTAL DATA

Model predictions have been compared with reported JPL–WINDRAD measurements obtained in circular flights at a constant observation angle [4, p. 89], [5, pp. 1181–1183]. To make the comparison more precise, because of the lack of information on the atmospheric conditions and the necessary corrections, WINDRAD measurements azimuthally averaged are compared to the apparent brightness temperature [Eq. (4)] computed using the present model, including ocean surface emission, scattered downwelling atmospheric temperature, upwelling atmospheric temperature, and atmospheric attenuation assuming a horizontally stratified clear atmosphere (U.S. standard atmosphere) and a flight altitude of 10 km. Results are shown in Figure 3. At 37 GHz, the agreement between predicted $T_{h,v0}$ is better than 6.5 K for all conditions, except at $\theta = 65°$ horizontal polarization, which can be most probably attributed to atmospheric contributions not properly modeled.

Figure 3 shows the azimuthal dependence of T_v, T_h, and U with respect to the upwind direction ($\phi = 0°$), at observation angles $\theta = 45$, 55, and 65°, $f = 37$ GHz, and $w = 9$ m/s. The agreement with JPL–WINDRAD measurements is quite good at $\theta = 55$ and 65°, although the second harmonic of T_h and T_v is a little bit underestimated at $\theta = 45°$. Figure 4 shows the importance of atmospheric effects when the azimuthal dependence of the surface emission is small. The atmospheric contribution is shown for the horizontal brightness temperature at 37 GHz, $w = 9$ m/s, and $\theta = 45°$ [Fig. 4(a)], and for the third Stokes parameter at 37 GHz, $w = 2.5$ m/s, and $\theta = 65°$ [Fig. 4(b)]. It appears that, around a 45° observation angle, the azimuthal variation exhibited by the modeled T_h [dotted line, Fig. 4(a)] is much smaller than the measured values. The agreement improves significantly after accounting for atmospheric effects, i.e., scattered atmospheric temperature and attenuation [solid line, Fig. 4(a)]. Figure 4(b) illustrates an interesting phenomenon: the significance of the uncertainties in Cox and Munk coefficients at low wind speeds. The dotted line represents the emission from the ocean calculated at 1.5 m/s wind speed [Fig. 4(b)], within the ± 1 m/s measurement uncertainty, and the solid line represents the result of adding the scattered downwelling atmospheric temperature and the attenuation. The azimuthal dependence of U_{sc} and T_{sch} must be considered in all cases, although it is not always as important as in these two examples. As expected, T_{scv} is usually much smaller than $e_v(\theta, \phi) \cdot T_s$ since the vertical reflection coefficient is lower.

6. CONCLUSIONS

This paper presents the results of an improved analytical Kirchhoff model under the stationary phase approximation for the first three elements of the Stokes vector (T_h, T_v and U, $V = 0$) of ocean surface emission. Ocean slopes are modeled by a Cox and Munk probability density function (pdf), including upwind/cross-wind rms slopes, skewness, and peakedness terms. It is found that the asymmetry of upwind/cross-wind rms slopes is responsible for the azimuthal second harmonic of the Stokes vector, while skewness terms are responsible for the first azimuthal harmonic, and peakedness terms have a negligible impact. The main advantages of this approach are its simplicity and its independence of the choice of any particular tuning parameter. Simulation results compare favorably with JPL–WINDRAD measurements. The analysis has also demonstrated the importance of the polar-

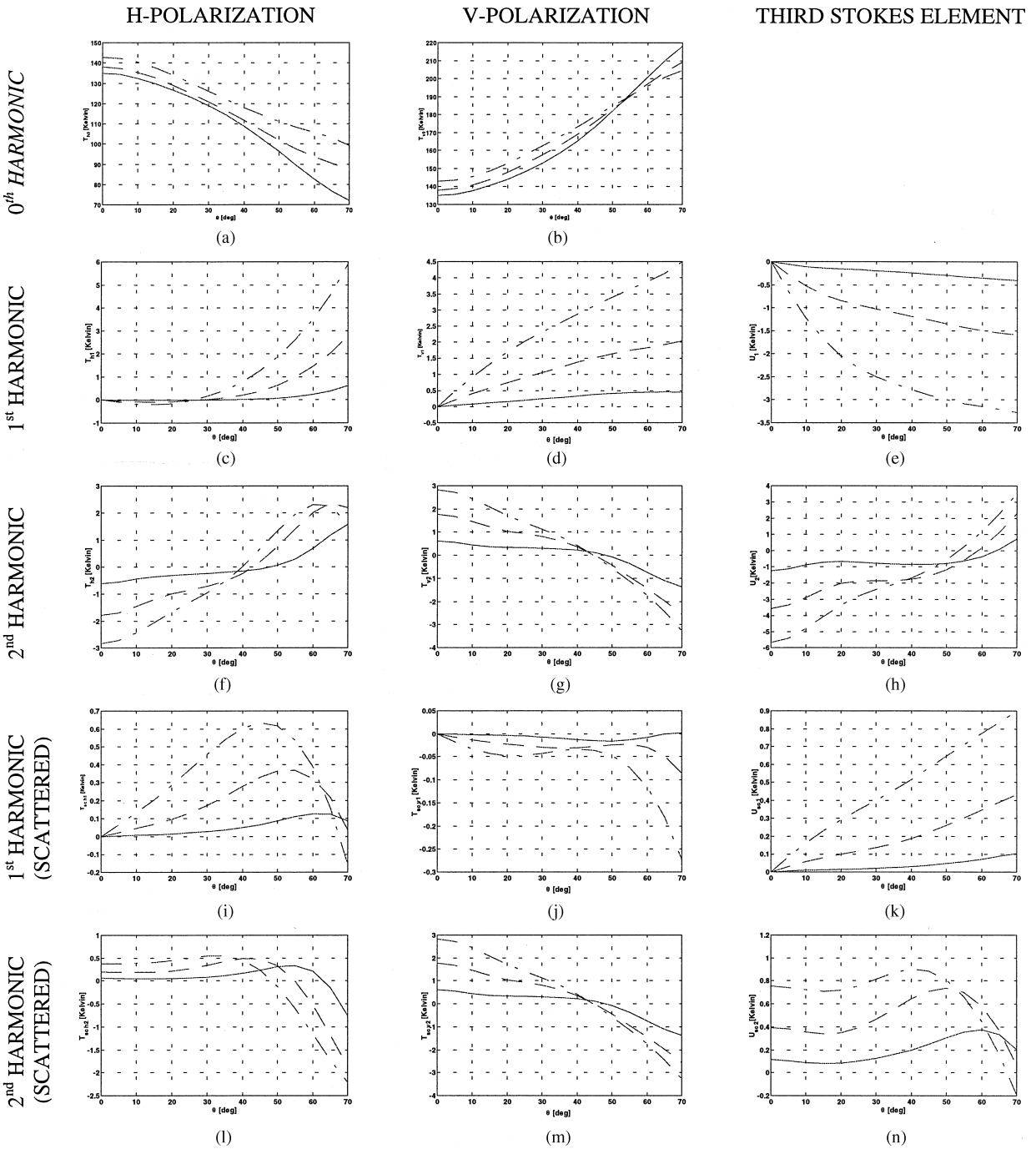

Figure 2 Computed azimuthal harmonics of T_h, T_v, U, T_{sch}, T_{scv}, and U_{sc} at 37 GHz and $w = 5$ m/s (solid), 10 m/s (dashed), and 15 m/s (dashed–dotted). SST = 12°C, SSS = 33 psu, $T_{DN}(0°) = 22.8$ K

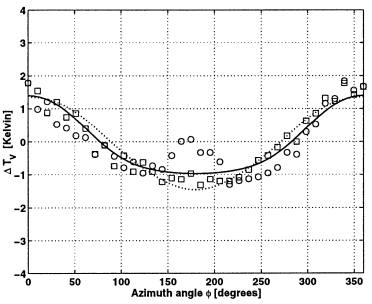

(a) T_{v0} = 168.8 K / 175.0 K (19 GHz)
188.9 K / 195.3 K (37 GHz)

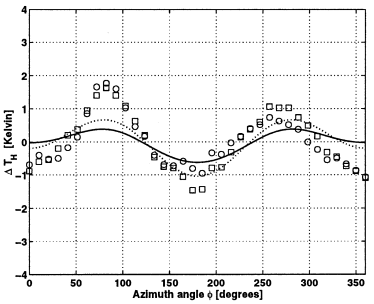

(b) T_{h0} = 121.3 K / 121.4 K (19 GHz)
144.2 K / 144.6 K (37 GHz)

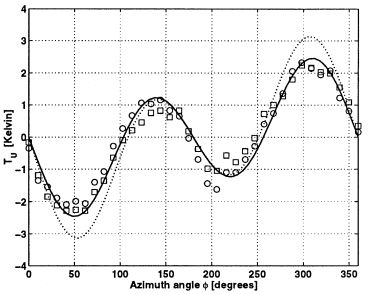

(c) U_0 = 0 K

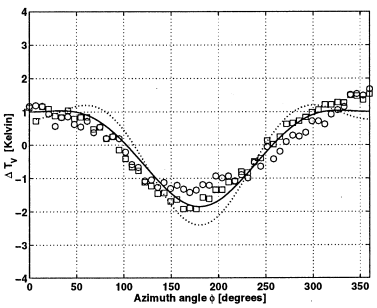

(d) T_{v0} = 186.7 K / 192.6 K (19 GHz)
205.0 K / 210.1 K (37 GHz)

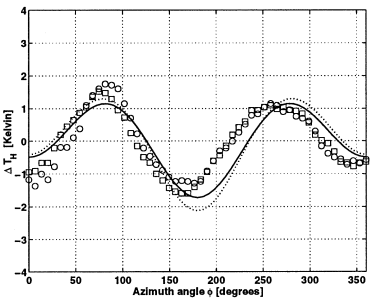

(e) T_{h0} = 117.4 K / 120.4 K (19 GHz)
141.5 K / 146.9 K (37 GHz)

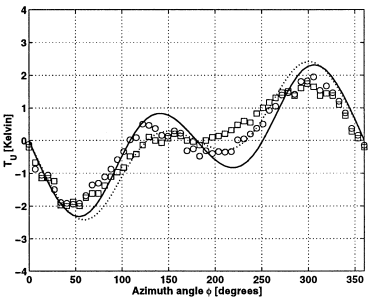

(f) U_0 = 0 K

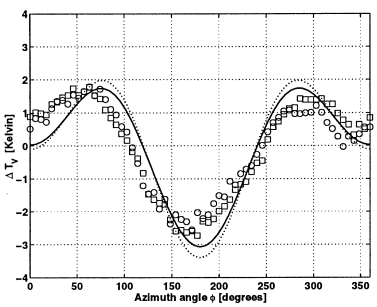

(g) T_{v0} = 204.4 K / 212.8 K (19 GHz)
219.9 K / 224.7 K (37 GHz)

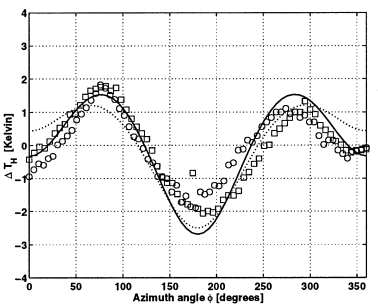

(h) T_{h0} = 116.7 K / 126.9 K (19 GHz)
142.5 K / 154.4 K (37 GHz)

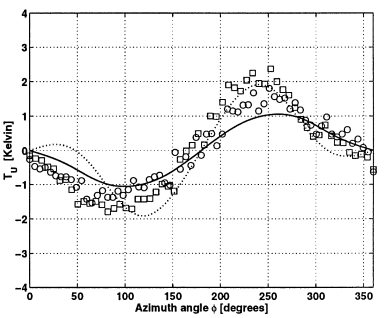

(i) U_0 = 0 K

Figure 3 Comparison of JPL–WINDRAD measurements with numerical simulations. Data: ○ 19 GHz, ×37 GHz. Simulations: solid line 19 GHz, dotted line 37 GHz. Observation angles: (a)–(c) 45°, (d)–(f) 55°, (g)–(i) 65°. (a), (d), (g) T_v, (b), (e), (h) T_h, and (c), (f), (i) U. SST = 12°C, SSS = 33 psu, and the U.S. standard clear atmosphere. Wind speed: 9 m/s at θ = 45, 55, and 65°. Bottom: $T_{v,h0}$ from data/$T_{v,h0}$ from model assuming U.S. standard atmosphere at 19 and 37 GHz. U_0 = 0 for all w

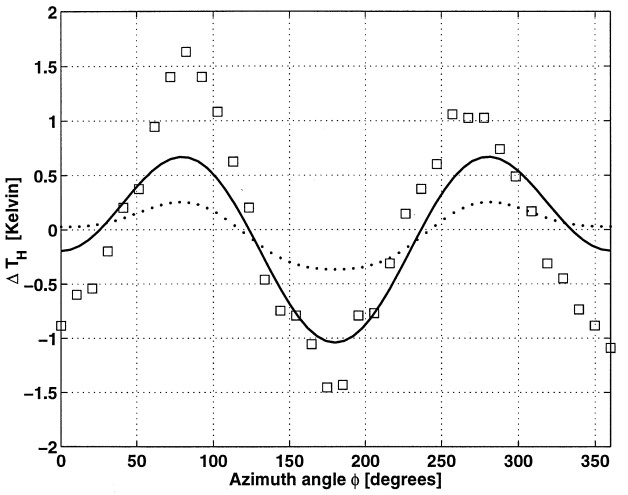

(a)

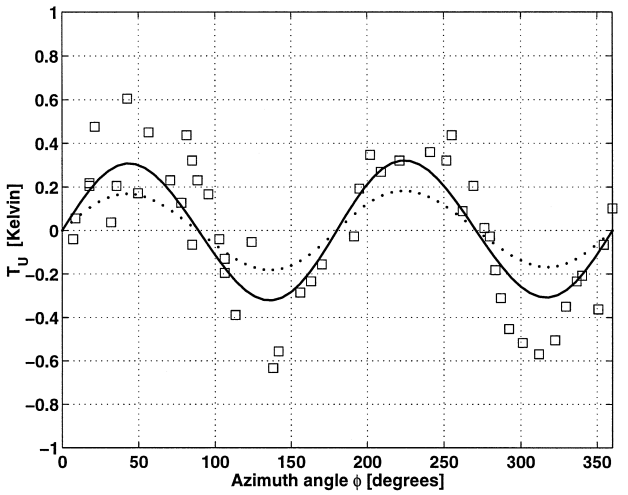

(b)

Figure 4 Atmospheric contribution to the azimuthal dependence of the Stokes vector at 37 GHz: (a) ΔT_h at $\theta = 45°$ and $w = 9$ m/s. (b) U at $\theta = 65°$ and nominal wind speed $w = 2.5$ m/s. Dotted line: ocean emission attenuated by the atmosphere. Solid line: ocean emission and downwelling atmospheric temperature scattered over the ocean surface, attenuated by the atmosphere up to 10 km

ization in the downwelling atmospheric brightness temperature induced by the scattering on the ocean surface, which is especially important for T_h and U at low wind speeds and/or observation angles near 45°.

ACKNOWLEDGMENT

This work was performed during A. Camps' sabbatical leave at the Microwave Remote Sensing Laboratory, University of Massachusetts, Amherst.

REFERENCES

1. F.J. Wentz, Measurement of oceanic wind vector using satellite microwave radiometers, IEEE Trans Geosci Remote Sensing 30 (1992), 960–972.
2. A.J. Gasiewski and D.B. Kunkee, Polarized microwave emission from water waves, Radio Sci 29 (1994), 1449–1466.
3. S.H. Yueh, R. Kwok, F.K. Li, S.V. Nghiem, W.J. Wilson, and J.A. Kong, Polarimetric passive remote sensing of ocean wind vectors, Radio Sci 29 (1994), 799–814.
4. S.H. Yueh, W.J. Wilson, F.K. Li, S.V. Nghiem, and W.B. Ricketts, Polarimetric measurements of sea surface brightness temperatures using an aircraft K-band radiometer, IEEE Trans Geosci Remote Sensing 33 (1995), 85–92.
5. S.H. Yueh, W.J. Wilson, F.K. Li, S.V. Nghiem, and W.B. Ricketts, Polarimetric brightness temperatures of sea surfaces measured with aircraft K- and Ka-band radiometers, IEEE Trans Geosci Remote Sensing 35 (1997), 1177–1187.
6. K.M. St. Germain and P.W. Gaiser, Spaceborne polarimetric microwave radiometry and the Coriolis WindSat system, IEEE 2000 Aerospace Conf Proc, Big Sky, MT, Mar. 2000 (CD-ROM edition, ISBN: 0-7803-5847-3).
7. S.H. Yueh, Modeling of wind direction signals in polarimetric sea surface brightness temperatures, IEEE Trans Geosci Remote Sensing 35 (1997), 1400–1418.
8. V.G. Irisov, Small-slope expansion for thermal and reflected radiation from a rough surface, Waves in Random Media 7 (1997), 1–10.
9. J.T. Johnson and M. Zhang, Theoretical study of the small slope approximation for the ocean polarimetric thermal emission, IEEE Trans Geosci Remote Sensing 37 (1999), 2305–2316.
10. D.B. Kunkee and A.J. Gasiewski, Simulation of passive microwave wind direction signatures over the ocean using asymmetric-wave geometrical optics model, Radio Sci 32 (1997), 59–78.
11. J.T. Johnson, R.T. Shin, J.A. Kong, L. Tsang, and K. Pak, A numerical study of the ocean polarimetric thermal emission, IEEE Trans Geosci Remote Sensing 37 (1999), 8–20.
12. J. Noll, Small perturbation model simulations applied to POLRAD-96, Proc Int Workshop Polarimetric Radiation Experiment, POLRAD'96, WPP-135, ESTEC, Noordwijk, The Netherlands, Apr. 1997, pp. 19–23.
13. A. Stogryn, The apparent temperature of the sea at microwave frequencies, IEEE Trans Antennas Propagat AP-15 (1967), 278–286.
14. W.H. Peake, Interaction of electromagnetic waves with some natural surfaces, IRE Trans Antennas Propagat (special suppl) AP-7 (1959), S324–S329.
15. A. Stogryn, Electromagnetic scattering from rough, finitely conducting surfaces, Radio Sci 2 (new ser) no. 4 (1967), 415–428.
16. T.T. Wilheit, A model for the microwave emissivity of the ocean's surface as a function of wind speed, IEEE Trans Geosci Electron GE-17 (1979), 244–249.
17. C. Cox and W. Munk, Measurement of the roughness of the sea surface from photographs of the sun's glitter, J Opt Soc Amer 44 (1954).
18. P.M. Smith, The emissivity of sea foam at 19 and 37 GHz, IEEE Trans Geosci Remote Sensing 26 (1988), 541–547.
19. S.C. Reising and A. Camps, A model for the wind direction signature in the Stokes emission vector from the ocean surfaces at microwave frequencies, Proc Int Geosci Remote Sensing Symp, IGARSS 2000, HI, July 2000.
20. E.C. Monahan and M. Lu, Acoustically relevant bubble assemblages and their dependence on metereological parameters, IEEE J Oceanic Eng 15 (1990), 340–349.
21. E.C. Monahan and I.G. O'Muircheartaigh, Whitecaps and the passive remote sensing of the ocean surface, Int J Remote Sensing 7 (1986), 627–642.
22. C.P. Yeang, S.H. Yueh, K.H. Ding, and J.A. Kong, Atmospheric effect on microwave polarimetric passive remote sensing of ocean surfaces, Radio Sci 34 (1999), 521–537.
23. A. Camps, M. Vall-Ilossera, N. Duffo, F. Torres, J. Bará, I. Corbella, and J. Capdevila, "Polarimetric radiometry of rain events: Theoretical prediction and experimental results," Microwave radiometry and remote sensing of the earth's surface and atmosphere, P. Pampaloni and S. Paloscia (Editors), VSP, 2000, pp. 325–335.